# Thin-film image sensors with a pinned photodiode structure

Jiwon Lee[1,3†], Epimitheas Georgitzikis[1†], Yannick Hermans[1], Nikolas Papadopoulos[1], Naresh Chandrasekaran[1], Minhyun Jin[1,4], Abu Bakar Siddik[1,2], Florian De Roose[1], Griet Uytterhoeven[1], Joo Hyoung Kim[1], Renaud Puybaret[1], Yunlong Li[1], Vladimir Pejovic[1], Gauri Karve[1], David Cheyns[1], Jan Genoe[1,2], Paweł E. Malinowski[1], Paul Heremans[1,2], and Kris Myny[1,2]

[1]imec, Leuven, 3001, Belgium
[2]ESAT, KU Leuven, 3001 Heverlee, Belgium
[3] Department of Photonics and Nanoelectronics, BK21 FOUR ERICA-ACE Center, Hanyang University ERICA, Ansan 15588, Korea
[4]Dongguk University, Seoul, Korea
[†]These authors contributed equally
(Corresponding author: Jiwon Lee, e-mail: leejiwon1@hanyang.ac.kr)

## ABSTRACT

Image sensors made using silicon complementary metal–oxide–semiconductor (CMOS) technology can be found in numerous electronic devices, and typically rely on pinned photodiode structures. Photodiodes based on thin films can have a high absorption coefficient and a wider wavelength range than silicon devices. However, their use in image sensors has been limited by high kTC noise, dark current and image lag. Here, we show that thin-film-based image sensors with a pinned photodiode structure can have comparable noise performance to a silicon pinned photodiode pixel. We integrate either a visible to near-infrared organic photodiode, or a short-wave infrared colloidal quantum dot photodiode, with a thin-film transistor and silicon readout circuitry. The thin-film pinned photodiode structures exhibits low kTC noise, suppressed dark current, high full well capacity and high electron-to-voltage conversion gain, while preserving the benefits of the thin-film materials. An image sensor based on the organic absorber has a quantum efficiency of 54% at 940 nm and read noise of 6.1e-.

## INTRODUCTION

Thin-film-based image sensors can offer high absorption over a broad wavelength spectrum and can potentially be monolithically co-integration with readout circuits made using complementary metal–oxide–semiconductor (CMOS) or thin-film transistors (TFTs). Thin-film devices based on organic semiconductors have, for example, demonstrated a ten- to hundred-fold higher absorption coefficient in the visible range than silicon[1]; devices based on colloidal quantum dots (QDs) are sensitive in the short-wave to mid-wave infrared[2–5]; and devices based on metal-organic perovskites can be used for direct absorption of high energy radiation[6]. 8K resolution cameras using organic photodiodes[7,8] and X-ray image sensors using organic or perovskite photodiodes have also been created[9–11], as have commercial short-

wave infrared image sensors based on QDs[12–15]. However, applications for thin-film based image sensors are currently limited to those that are challenging to achieve with silicon-based devices because thin-film based image sensors have inferior noise performance than silicon.

The earliest implementation of CMOS image sensors (CISs) used a passive pixel sensor (PPS) structure[16,17], which was uncompetitive with the dominant image sensor technology at the time — the charge coupled device (CCD). The CCDs used a pinned photodiode (PPD) structure[18], which can fully deplete the photodiode storage and better transfer charges to the readout circuit, resulting in improved image quality. In comparison, early CISs had inferior noise performance due to fixed pattern noise and low charge-to-voltage conversion gain[19].

The development of active pixel sensors (APS)[20] in CIS with an in-pixel buffer improved photon-to-electron conversion gain, while retaining the original advantages over CCDs being lower power consumption and compatibility with other CMOS technologies (enabling co-integration of the peripheral and readout circuit on the same chip). However, they still exhibited worse image quality compared to CCDs[19,21]. This was mainly due to high dark current caused by extension of the photodiode to the silicon interface and kTC noise generated during the photodiode reset. Both these phenomena result from the photodiode connecting directly to the metal contact of the in-pixel source follower and reset transistor. This contact area and the top silicon surface contain a high density of defect states. Additionally, kTC noise is created when the charge storage node cannot be fully depleted, which causes reset level changes from frame to frame. The full well capacity (FWC) of the photodiode — which determines the dynamic range and the charge-to-voltage conversion gain of the sensor — is also interlinked since the photodiode is itself part of the conversion node. This introduces a trade-off: a large capacitance, for example, is required for high FWC and low capacitance favours high conversion gain. These early implementations of CMOS image sensors also had high image lag because the reset level potential of the photodiode was affected by the state of the photodiode at the end of the previous integration phase.

To overcome these issues, pixel sensors were extended from previous designs, which had been based on three transistor gates (referred to as '3T' pixel), to a four-gate design ('4T' pixel) that incorporated the PPD structure[19,22,23]. This configuration uses a p+np photodiode structure with the sandwiched n region, which is used as storage, being separated from the readout node by an extra transistor. By fully depleting the storage node during reset operation, the effect of the previous state (image lag) and the kTC noise can be reduced. Also, the separation of the storage node from the surface by the p+ region, and from the metal contact by the additional transistor, minimizes dark current, as the photodiode is isolated from the defective surface or the contact region. The adoption of the PPD structure to CMOS image sensors allowed them to compete with CCD image sensors and they are now the standard technology for consumer imaging devices[22–24].

Thin-film photodiodes currently suffer from the same problems as early CMOS image sensors: high noise levels, high dark currents, non-optimized gain versus full well capacity (FWC), and image lag. A pixel structure using negative feedback operation during reset or storing reset level voltage by adding a capacitor in pixel have been implemented to suppress kTC noise and image lag[7,8,25,26], but the design is complex and still has higher dark current and unoptimized conversion gain/FWC compared to CMOS image sensors. Adding a capacitive transimpedance amplifier (CTIA) can suppress dark current and optimize gain/FWC, but fails to eliminate kTC noise and requires a relatively large pixel and high static power[13].

In this Article, we report a thin-film-based image sensor with a pinned photodiode pixel structure (TF-PPD). We use either an organic photodiode sensitive to visible to near-infrared (NIR) wavelengths, or a quantum dot photodiode sensitive to short-wave infrared (SWIR). In both cases, high linearity is measured for varying integration time, indicating efficient transfer of charges, and full depletion of the photodiode node prevents the generation of kTC noise and image lag. In comparison to thin-film imagers with the same photodiode material and a conventional 3T pixel structure, our 4T TF-PPD pixel has a two order of magnitude decrease in dark read-noise (114.7e- to 6.1e-), and a five times improvement in conversion gain.

## TF-PPD PIXEL STRUCTURE

Figure 1 shows the proposed thin-film photodiode and thin-film transistor (TFT) hybrid PPD structure; in top view (Fig. 1a) and cross-sectional view (Fig. 1b). In comparison to the conventional thin-film-based pixel structure, where the photodiode is connected directly to the readout (Supplementary Figure 1)[7,8,13–15,27], a TFT structure is included serving two different purposes: it operates as a transfer gate (TG) and it constitutes part of the photogate (PG)[22,28]. The selected semiconductor, indium gallium zinc oxide (IGZO), acts both as the electron transport layer (ETL) of the photodiode and as the channel layer for the transfer gate TFT, thanks to its relatively high electron mobility[29]. Two types of TF-PPD devices are implemented to confirm operation of the device, using either colloidal QDs or organic semiconductor as photo-absorption materials, using different material stacks. Finally, image sensor operation with the proposed PPD pixel structure is demonstrated by implementing the IGZO TFT on top of a fully processed 130 nm CMOS readout chip, which is followed by the OPD integration. The IGZO transistor integration scheme is based on a bottom-gate configuration.

The source of the TFT is directly contacted to the photodiode to collect the generated electrons, while the drain is connected to the readout transistors. The drain node is constituted as a floating diffusion (FD) node where the photogenerated charges are converted to a voltage level. The gate of the TFT is controlled by external biasing (TG) to connect or disconnect the photodiode and the FD. A photogate is included underneath the source node of the TFT to control the potential of IGZO and hence the field distribution in the photodiode. This structure can be understood as a back-side illuminated photogate pixel structure. By realizing a back-gated photogate structure, the photodiode materials can be deposited directly on top of the IGZO channel, and the incoming light will reflect on the metal gate towards the photodiode to boost the absorption in the thin-film active layers. Thanks to the large bandgap of IGZO, the depleted surface of the semiconductor near the gate dielectric does not increase the dark current, which is the main drawback of the surface channel silicon photogate[30]. Therefore, generated charges can be stored in the IGZO at the interface to the gate dielectric which enables high full well capacity by using high density gate capacitance. By controlling the PG potential, the photodiode can be negatively biased to successfully separate generated charges and subsequently collect photoelectrons in the IGZO layer. Also, with the help of the PG bias, all the collected photoelectrons are fully transferred to the floating diffusion node when TG is turned on following the lateral potential difference. The potential distribution of the proposed device is simulated using Technology Computer-Aided Design (TCAD) which confirmed the operation of the TG and PG (Supplementary Figure 2).

Figure 1c demonstrates the operation of the proposed thin-film PPD pixel. Immediately after the thin-film PPD reset, no charges remain, ensuring isolation from the previous frame and hence no kTC noise is

observed. During the integration time, the photo-generated electrons are stored in the IGZO on top of the PG with the help of the positive bias applied to the PG while the TG is turned off. The stored charges are transferred to the FD node by turning on TG and are read out by pixel electronics. The voltage difference with respect to the reset level, which is sampled right before charge transfer, defines the intensity of the light detected. This process of sampling the FD node twice, once with the reset level and once with the signal level, is called correlated double sampling (CDS) operation, and is a conventional technique to suppress reset noise (kTC) from FD node and FPN arising from the variation of the pixel transistors.

In a PPD pixel, the reset and signal are available almost simultaneously, enabling on-chip CDS operation at the circuit level. On the contrary, in the case of a general 3T pixel structure, the reset and signal are output at intervals of integration time. This means that to remove the kTC noise, frame memory and per-pixel correction in the digital domain are required which increases system complexity enormously. A TF-PPD pixel has the same electrical pixel components as a conventional silicon-PPD pixel[23] as can be seen in Figure 1b. The reset (RST) transistor sets the FD node to the reference potential, the source follower (SF) buffers the FD voltage to the output node, and the select (SEL) transistor connects the pixels to the subsequent readout chain. These three transistors are implemented on silicon.

## TF-PPD FABRICATION AND CHARACTERIZATION

To demonstrate the operation of the proposed thin-film PPD architecture, two types of photodiodes, an organic photodiode (OPD) and a quantum dot photodiode (QDPD) (Figure 2a-e), are co-integrated with IGZO TFT (Figure 2f-h). For the OPD, a bulk-heterojunction system is used, composed by a donor-acceptor blend with high spectral sensitivity from the visible up to 1000 nm (Supplementary Figure 3a). In the case of the QDPD, PbS based colloidal quantum dots are used as the absorber material. The nanoparticles used have a size of 5.5 nm corresponding to an absorption peak at the wavelength of 1425 nm while in a colloidal solution phase (Supplementary Figure 3b). To form a photodiode, a junction between an n-type and a p-type QD layers is formed by appropriate ligand exchange engineering (see methods section)[31–33] . Figure 2 c-e shows the measured photodiode characteristics optimized to work with IGZO as ETL. Two different test pixel sizes are designed, being 7.5x7.5 $\mu m^2$ and 10x10 $\mu m^2$, while the size of the PG (assumed to define the photosensitive part of the device) occupies about 95% of the device footprint for the case of the 10x10 $\mu m^2$ pixel. As a reference, a conventional photodiode pixel having an active area of 10x10 $\mu m^2$ is included (Figure 3d, e). For the case of the 10 $\mu m$ pixel, the transfer gate has width over length of 7.6 $\mu m$ / 0.4 $\mu m$ while the contact size connecting the IGZO layer to the drain metal is 0.3x0.3 $\mu m^2$. The thickness of IGZO and $Al_2O_3$ dielectric are designed to be 12nm each. To enable a practical readout, 500-unit PPD structures are connected in parallel. This parallel output node is then either connected to the parameter analyzer to measure DC characteristics or to the off-chip transimpedance amplifier to test transient response.

Figure 3a shows a SEM picture of the fabricated TF-PPD device, and Figure 3b a TEM picture of the cross-section of the device. The reference photodiode was optimized on the TF-PPD test structure to yield a thin-film stack as depicted in Figure 2a. The main target was to assemble a photodiode stack with a low dark current density, while still maintaining a high external quantum efficiency (EQE) over a wide wavelength range. IGZO was herein used as an electron transport layer (ETL). The morphology of the IGZO ETL and the organic blend deposited on top of it is characterized by atomic force microscopy (AFM) showing uniform films with roughness of 2.2 nm and 0.9 nm respectively (Supplementary Figure 4). IGZO

4

has been already proven to be an effective ETL for organic photodiodes and has been also used in combination with PbS QDs for the realization of photoconductors[34,35]. Here, for the first time we incorporate IGZO in a p-n junction with PbS QDs to form a photodiode configuration. Due to the dual role of IGZO as ETL and transfer gate it is crucial that all the photogenerated electrons are efficiently transferred. Thus, in both cases a staggered photodiode band alignment design is implemented (Figure 2b). To ensure the proper band configuration, the IGZO layer composition and energy levels are characterized by X-ray photoelectron spectroscopy (XPS) and ultraviolet photoelectron spectroscopy (UPS) respectively (Supplementary Figure 5 and 6). By the addition of an organic hole transport multilayer we could minimize the dark current and achieve a dark current density of $2.6 \times 10^{-8}$ A/cm² and $1.1 \times 10^{-7}$ A/cm² at -3 V for the case of OPD and QDPD respectively (Figure 2c). An EQE above 40 % could be attained from 600 nm to 970 nm under an applied bias of -3 V (Figure 2d) for the case of OPD, resulting in a photodiode sensitive in the visible to near infrared (NIR) region (Supplementary Figure 7a). Moreover, 27% of EQE could be achieved at a wavelength of 1450 nm for the case of the QDPD enabling SWIR imaging (Supplementary Figure 7c). The developed back-gated IGZO transistor with back source/drain contact is measured to have threshold voltage of -0.5V, subthreshold swing of 90 mV/dec, and on-off ratio higher than $10^4$ (Figure 2f-h).

The fabricated OPD based TF-PPD is measured under constant TG bias (VTG) while varying the PG bias (VPG) (Figure 3f), and under constant VPG while varying the VTG (Figure 3g). From Figure 3f, the operation of TG can be confirmed by the following observation: when the TG voltage is low, the photodiode is not connected to the FD, so the photocurrent is low, and when the TG voltage is high, a high photocurrent is measured. As can be seen from Figure 3g, when TG is fully open, the sensitivity of the device increases with VPG and eventually saturates to the same sensitivity level as the reference diode. Even when the photogate is not connected to the FD, the current is higher than in the dark because the FD also has a small parasitic photodiode which responds to light. From this DC measurement, the operation of PG and TG can be confirmed. The sensitivity of the proposed device (Figure 3h) reaches that of the reference diode, which proves that the proposed device does not cause any loss of sensitivity.

The transient response of the developed device is measured with off-the-shelf CTIA and FPGA integrated on a printed circuit board (PCB) (see Methods section). As shown in Figure 4a, 500 TF-PPD devices are connected in parallel to the CTIA and the charges collected in the photogate are transferred to the input node of the CTIA. The output of the CTIA is monitored by an oscilloscope. The reset level is sampled right after turning off RST, followed by the signal level sampling right after TG is turned off. The output representing the amount of the incident light signal is calculated by subtracting the reset level from the signal level, as in a CDS operation. By changing the integration time, a linear input-to-output relation is measured as expected for the case of both OPD and QD-PD based TF-PPD (Figure 4 b, c, d, e), indicating that the generated charges are successfully transferred and read out.

To verify the full depletion of the TF-PPD after reset (which prevents kTC noise and the effect of the previous frame), the image lag is measured (Figure 4f). After illuminating the device under test (DUT) for a single frame by flashing an LED, it is kept under dark for the subsequent frames[36]. The remaining charges after the illuminated frame are transferred during subsequent frames. If the photodiode is fully depleted, there will be no charges transferred in the subsequent frames. The test result presented in Figure 4f shows that the remaining charges decrease with longer transfer time ("TG-on time"). The number of charges transferred during the subsequent frame is normalized to the number filled in the illuminated frame. At

5

TG-on time of 50 µs, for the case of the OPD based TF-PPD, the image lag is measured to be 3.5% and 1.5% for 10 µm and 7.5 µm pixels, respectively. From this measurement, it can be concluded that during the transfer operation most of the charges in the photogate are transferred to the floating diffusion, so that the photogate empties almost completely. However, some charges are still left after relatively long transfer times and QD based TF-PPD showed even worse image lag performance. The remaining image lag, even accounting for the mobility of IGZO (around 10 cm$^2$/Vs), is believed to be caused by traps in the channel and the 200 nm gap between the photogate and the transfer gate in the current design. The unbiased gap region can cause a potential barrier which prevents the full depletion of the device[37,38]. Further research is required to pinpoint the exact cause of the remaining image lag.

## IMAGE SENSOR ARRAY DEMONSTRATION

A prototype image sensor array together with the new TF-PPD pixel structure was fabricated by using an 0.13 µm CMOS process. A back-gated IGZO TFT is integrated on top of the fully processed silicon ROIC, followed by the processing of the optimized OPD. Figure 5a shows a prototype image sensor and camera demonstration example. The array consists of 64x64 pixels with 5 µm pixel pitch. Figure 5b shows a sample image captured with the prototype image sensor. The operation of the TF-PPD based imager chip is confirmed by measuring the output of the pixel source follower without going through the readout chain by enabling a test operation mode. Figure 5c shows the operation timing diagram and example output of the developed TF-PPD pixel directly with the test mode. The output voltage drops as the TG is turned on, proportional to the number of charges transferred from PG to FD. Figure 5d confirms the linear response of the image sensor, with a measured conversion gain of 58µV/e-, which is about 5 times higher compared to the conventional 3T photodiode pixel (11 µV/e-) structure[27]. This can be attributed to the isolation of the photodetector area from the FD region, which results in a lower FD capacitance. On top of the kTC noise reduction due to the full depletion of the photogate, this high CG further improves input referred noise by suppressing noises from subsequent readout chain. The input referred dark read-noise is reduced to 6.1e- (cf. 114.7e- of conventional 3T pixel with the same photodetector material) thanks to the TF-PPD operation with minimum additional complexity of one added TFT (TG) as shown in Figure 5f. Even with the addition of the in-pixel component, the proposed TF-PPD based 4T pixel is beneficial for pixel scaling by enabling pixel transistor sharing (RST, SF and SEL), a technique widely used for conventional silicon CIS[23,39–41]. The quantum efficiency is measured to be 54% at 940 nm which is comparable to the value measured with a discrete photodiode. Dark current is reduced to 14.4 nA/cm$^2$ from the dark current of 60.1 nA/cm$^2$ of conventional 3T pixel (Figure 5g), thanks to the isolation of the photodiode from the defective silicon contact region which has a dark current contribution of about 10 fA[42]. The improvement is striking when comparing the images captured under the same conditions using the 4T and the 3T pixel sensors (Figure 5h). The lower noise and dark current, combined with the higher conversion gain lead to a brighter image with better image quality (also Supplementary Figure 11).

Table 1 summarizes the measured performance of the proposed TF-PPD image sensor and compares it to the published state-of-the-art thin-film and silicon-based image sensors. The TF-PPD image sensor compares favorably against the conventional approaches, mainly because of its distinct advantages such as low dark read noise and low dark current. The relatively low FWC is not limited by the TF-PPD itself but by the small FD capacitance of the current implementation. The FWC could be easily extended by using dual conversion gain technique which is being widely used for conventional CIS design[43,44]. The FWC of

the TF-PPD is expected to be about 5 times higher than that of 3T pixel structure thanks to higher MOS capacitance than photodiode junction capacitance.

## Conclusions and Outlook

We have reported a thin-film-based pinned photodiode image sensor that can offer correlated double sampling operation by fully transferring charges from the photogate to the floating diffusion node. The image sensors are created by integrating either an organic photodiode or a colloidal quantum dot photodiode with a photogate structure made of IGZO TFTs on top of CMOS readout circuits. The TF-PPDs show reduced kTC noise, increased conversion gain and reduced dark current compared to state-of-the-art thin-film imagers, while conserving the absorption advantages of thin-film photodiodes. Our photogate structure could potentially be integrated with various other thin-film materials, such as perovskites, that are currently limited by pixel architectures. The thin-film PPD structure addresses a key obstacle to the widespread adoption of thin-film photodetectors into commercial image sensors, while retaining the advantages — such as higher absorption coefficients and wider wavelength range — of thin-film absorbers over silicon-based sensors.

## Methods

**Device fabrication.** The silicon substrates including TiN bottom contacts and $Al_2O_3$ dielectric for the photodiode, TFT and TF-PPD passive devices were fabricated in a 200 mm semiconductor line. For the CMOS read-out electronics, a 130 nm node was used. The $Al_2O_3$ was deposited with atomic layer chemical vapor deposition (ALCVD). IGZO was deposited by sputtering using a target with In:Ga:Zn ratio 1:1:1 at room temperature with oxygen flow ratio in $O_2$+Ar sputtering gas mixture of 6%. After deposition the IGZO was patterned by photolithography and wet etched with oxalic acid. Then it was annealed in FOG atmosphere (Forming gas, 5% $H_2$ in $N_2$) at 180 °C for 30 minutes. In the next step the organic absorber was deposited by spin-coating using a donor-acceptor blend solution. After spun to dry a thin film of about 120 nm was achieved. For the QD absorber, films were deposited by spin-coating a solution of PbS QDs in octane (40 mg/ml) at 2500 rpm for 15 s. Solid-state ligand exchange process was performed by soaking the deposited film in a ligand solution, followed by spin-coating to dry the film. The film was then washed with pure ligand solvent twice to remove the excess ligands. For the n-type film $ZnI_2$-MPA mixture was used as the ligand while the p-type film was formed by using 1,4 benzenedithiol. The deposition, ligand exchange and washing processes were repeated multiple times until the required thickness was achieved. All the above steps were performed in a $N_2$ filled glovebox. Then the film was annealed in 80°C for 10 minutes under $N_2$. After the formation of the p-type film, the substrates were placed overnight in a dry-air box to enhance p doping, and afterwards returned to the glovebox for the remaining fabrication steps. Finally, a PolyTPD layer was formed by spin-coating a 6 mg/ml solution in chlorobenzene at 1000 rpm for 60 s. The film was then annealed at 80˚ C for 20 min. For the HTL, 100 nm of DNTPD (N1,N1'-(Biphenyl-4,4'-diyl)bis(N1-phenyl-N4,N4 -di-*m*-tolylbenzene-1,4-diamine) was deposited by thermal evaporation using a Kurt J. Lesker vacuum system. To reduce the contact resistance a 10 nm doped DNTPD layer with 5% F6TCNNQ was added on top. The ratio of DNTPD and F6TCNNQ was controlled by their evaporation rates. Finally, the ITO top transparent electrode was deposited by sputtering using an Angstrom engineering PVD system.

**Film Characterization.** Absorption spectra were measured using a Shimadzu UV1601 UV/VIS spectrophotometer. The film morphology was inspected by AFM using a Bruker atomic force microscope in the tapping mode in ambient air. The thickness profiles of the different films were measured using a Bruker DektakXT profiler. For the TEM cross-sections, specimen preparation was performed by focused ion beam with a Helios 450 system and the inspection was done with a Titan G2 60-300 TEM system.

**Device Characterization.** For the photodiode characterization current–voltage (I–V) curves were measured in a glovebox with an Agilent 4156 semiconductor parameter analyzer in the dark. The EQE spectra were recorded on a Stanford Research System model SR830 Lock-in Amplifier unit coupled with a monochromator and a 500 W Xenon lamp. The signal was first amplified by a Stanford Research System SR570 low noise current preamplifier. A calibrated Si photodiode with a known spectral response was used as a reference. The transient photoresponse, photocurrent linearity and capacitance–voltage measurements were performed using a Paios all-in-one system by Fluxim.
TFT measurements were performed in air using an Agilent 4156 semiconductor parameter analyzer.
The TF-PPD passive devices were characterized by a custom-made PCB probe card (Figure 10 in Supplementary Info).  The PCB integrated an off-the-shelf CTIA (Texas Instruments ACF2101) and FPGA (Xilinx Artix-7). The output of the CTIA is connected to the oscilloscope to be recorded. The device was illuminated by a Thorlabs M940L3 940 nm LED or by a M530L4 530 nm LED which were modulated by a Thorlabs DC2200 LED driver as a source of pulse signals.

## DATA AVAILABILITY

"The data that support the plots within this paper and other findings of this study are available from the corresponding author upon reasonable request".

## ACKNOWLEDGEMENTS

## AUTHOR CONTRIBUTIONS STATEMENT

J.W. and E.G. designed, performed and analyzed the experiments, P.H., P.M. and K.M. analyzed the experiments, N.P. and F.D.R. designed the experiments, M.J. and J-H.K. performed the experiments, Y.H., A.B.S., D.C., V.P. and G.U. performed the PD analysis and fabrication, N.C., R.P., Y.L. and G.K. performed the fabrication. All authors have reviewed the manuscript.

## COMPETING INTERESTS STATEMENT

There are no conflicts to declare.

## TABLES

Table 1: Measured characteristics of TF-PPD of this work compared to published state of art

| | PD Stack | photodetector / pixel structure | Pixel pitch (μm) | CG (μV/e) | FWC (e) | Dark RN (e) | Dynamic range (dB) | Dark current (nA/cm2) | Note * |
|---|---|---|---|---|---|---|---|---|---|
| **This work** | OPD | TF-PPD / 4T | 5 | 58.1 | 25,000* | 6.1 | 72.3 | 14.4 | *FD capacitance limited |
| **3T reference** | OPD | Photodiode / 3T | 5 | 11 | 90,000 | 114.7 | 57.9 | 60.1 | |
| **2018 Panasonic**[7] | OPD | Photodiode / 3T+active feedback | 3 | | 45,000 | 8.6 | 74.4 | | |
| **2021 STMicroelectronics**[15] | QDPD | Photodiode / 3T | 1.62 | | 10,000 | 21.3 | 53.4 | 250* | *@60C |
| **2020 Imec**[27] | QDPD | Photodiode / 3T | 5 | 8.3 | 470,000 | 33* | 83.1** | 300 | *Interframe digital CDS (x2 readout) ** Dual conversion gain |
| **2021 SWIR Vision Systems**[13] | QDPD | Photodiode / CTIA | 15 | | 550,000 | 65* | 78.5 | 8 | *Interframe digital CDS (x2 readout) |
| **2019 Sony** [45] | OPD | Photodiode / 3T | 2 | | | 6.5* | | | *Interframe digital CDS (x2 read), 27e @single read |
| **2021 Emberion** [46] | QDPD | Photodiode / CTIA | 20 | | | 200 | | 100* | *Dark current @0C, -0.86V |
| **2022 HiSilicon**[47] | QDPD | Photodiode / Direction injection | 15 | 10.0 / 1.42* | 350,000 | 110 | 70.1 | 17.8 | *Dual conversion gain High / low |
| **2015 NHK**[48] | Silicon | PPD / 4T | 2.45 | 80 | 10,005 | 7.68 | 62.3 | 0.13* | *@42C |
| **2017 Sony**[49] | Silicon | PPD / 4T | 5.86 | 30.3 | 30,450 | 4.62 | 76.4 | | |
| **2021 Sony**[50] | Silicon | PPD / 4T | 4.16 | 87.5 | 60,000 | 1.18 | 94.1* | | *Dual conversion gain |

## FIGURE LEGENDS/CAPTIONS
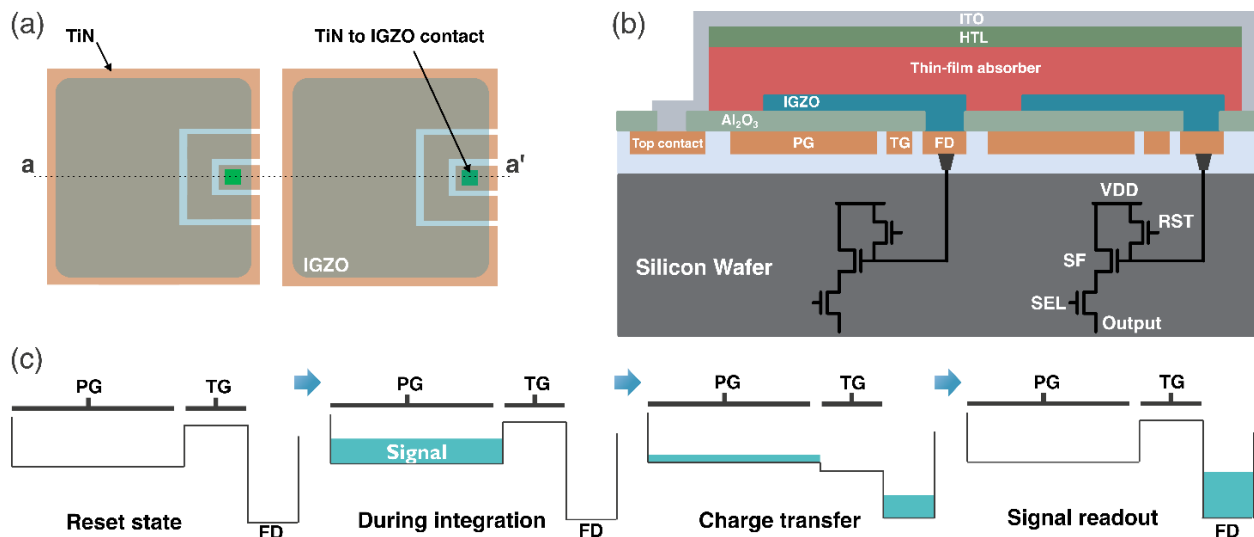


Figure 1: Simplified diagrams of two TF-PPD pixels side by side (a) in top view, (b) cross-sectional view along a-a' with additional top contact; (c) conceptual operation diagram of the proposed TF-PPD pixel. In our implementation, the thin-film absorber and HTL layers are not isolated between the pixels, all pixels have a common ITO anode contact, the IGZO TFT is gated from the backside, the IGZO TFTs and the organic photodiodes are processed on a 130-nm CMOS readout chip containing 3 transistors per pixel.
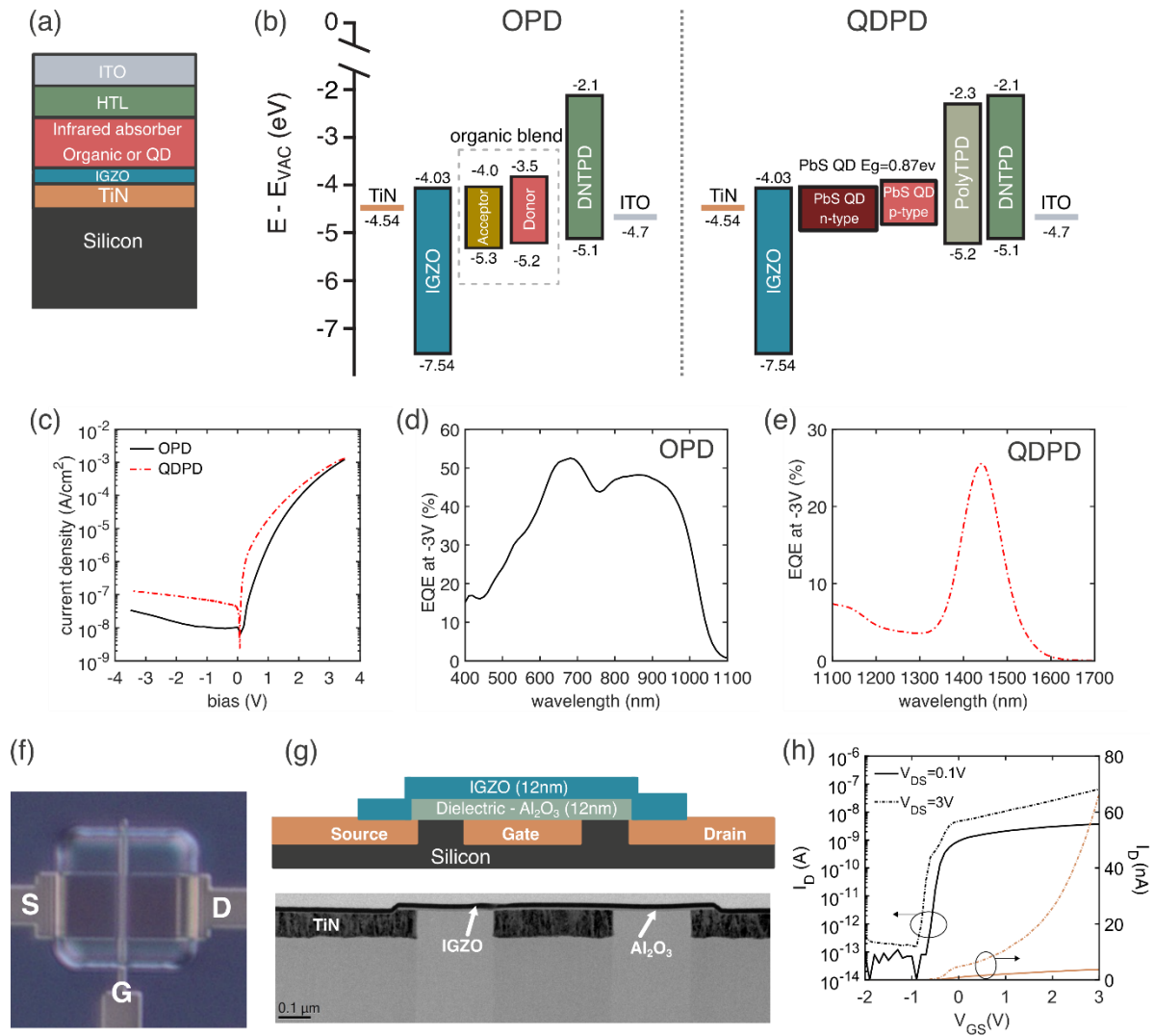
*Figure 2: Photodiode (a-e) and TFT (f-h) building blocks required for the TF-PPD pixel. (a) Device structure and (b) energy diagram of the NIR sensitive organic photodiode (OPD) and the SWIR sensitive quantum dot photodiode (QDPD). (c) Current-voltage curve under dark conditions and EQE (d) for the OPD and (e) for the QDPD. (f) Microscope image of the TFT test structures and (g) the corresponding cross-section schematic and TEM along the source-drain plane. Transfer characteristics of the TFT under $V_{Ds}$ of 0.1 V and 3 V (h). ETL and HTL are the electron and hole transport layer respectively.*
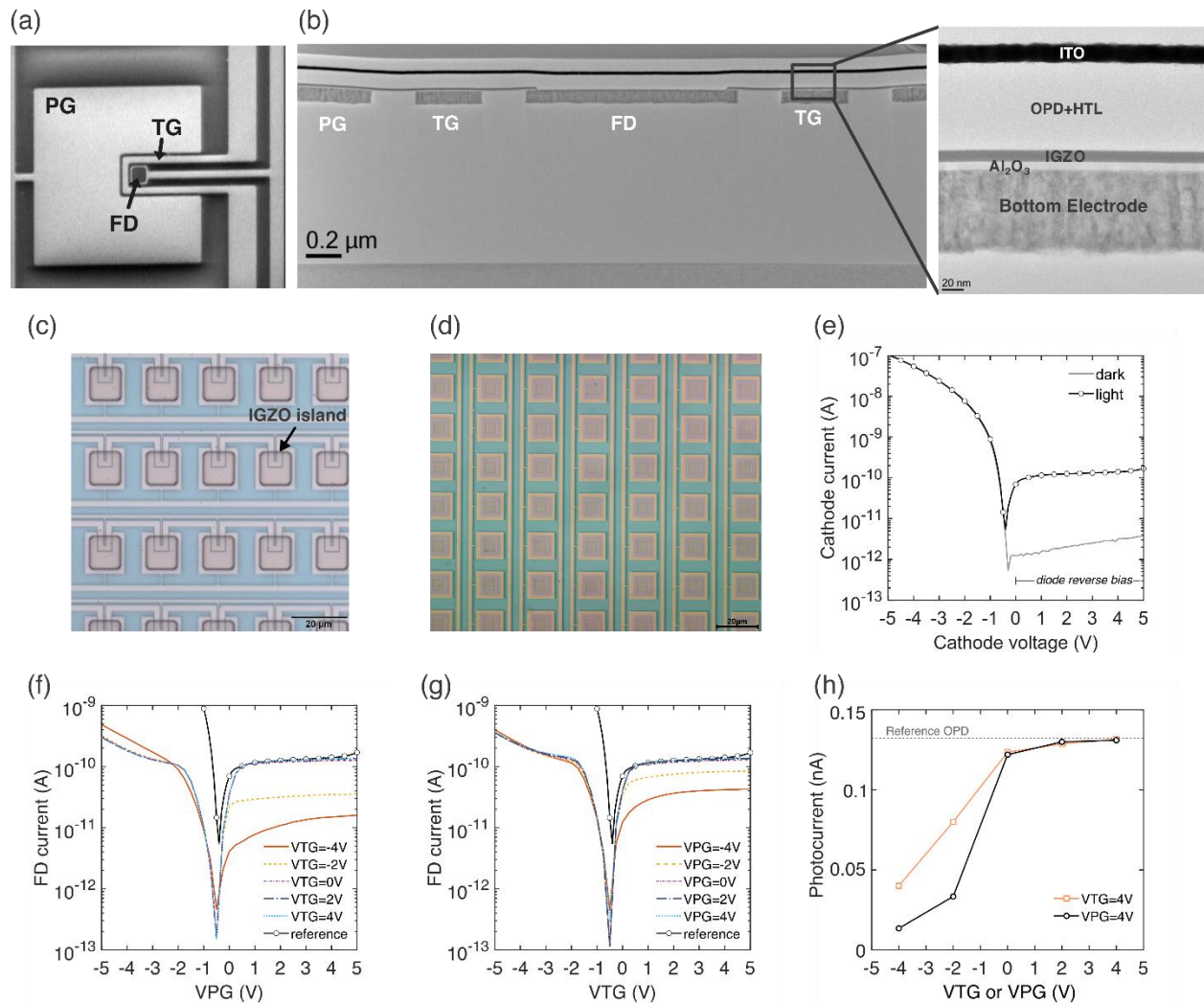
*Figure 3: The processed TF-PPD test structures (a) SEM picture of the processed TF-PPD pixel with OPD after dielectric deposition and patterning, (b) TEM picture of the cross-section of the full processed TF-PPD with OPD, (c) microscopic image of the TF-PPD test structures after IGZO deposition and patterning, (d) microscopic image of the reference OPD pixel array with an active area of 10x10 µm², (e) and the corresponding I-V characteristics under dark and light (530 nm, 1 mW/cm²), (f) FD current versus VPG at different VTG, (g) FD current versus VTG at different VPG, and (h) photocurrent comparison with reference OPD.*
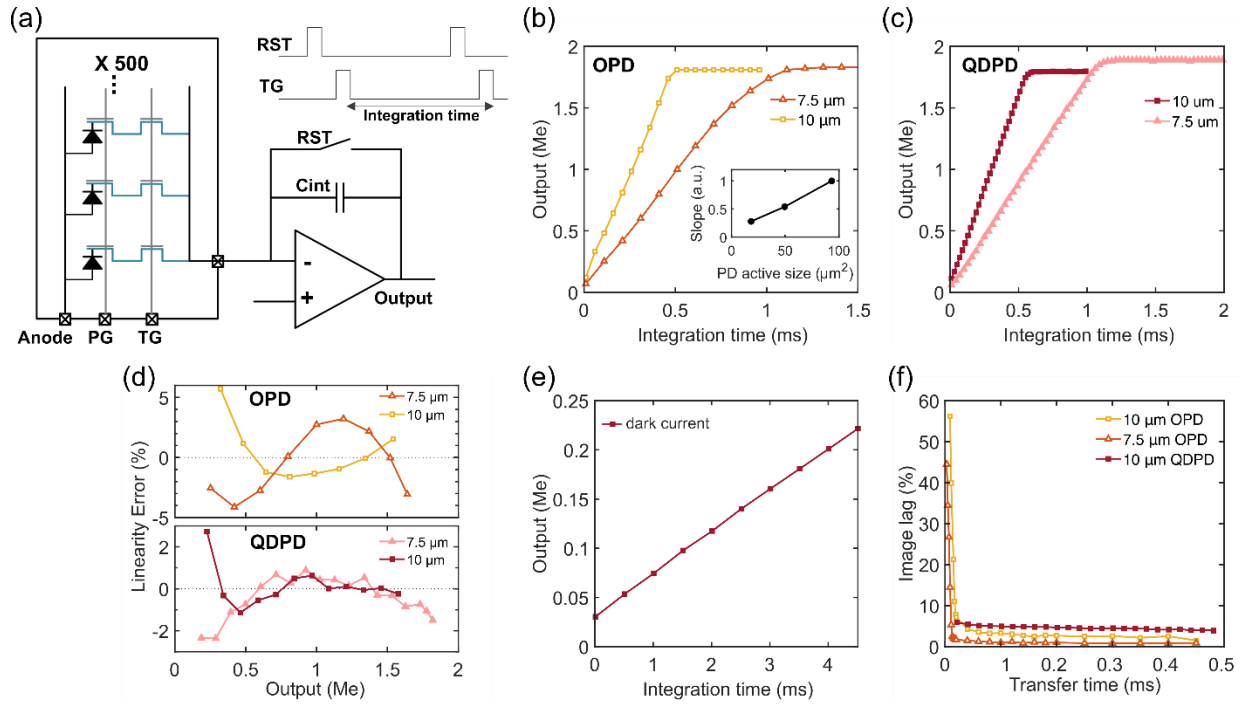
11

*Figure 4: Transient operation of the test TF-PPD structures (a) test setup; (b) measured number of output electrons versus integration time for the organic photodiode and (c) the quantum dot photodiode. (d) Calculated linearity error from 10% to 90% of saturation level for the organic photodiode and the quantum dot photodiode by computing least-squares linear regression. Dark current electrons for the 10 µm pixel QDPD for increasing integration time (e) and (f) image lag for the different photodiodes and pixel sizes.*
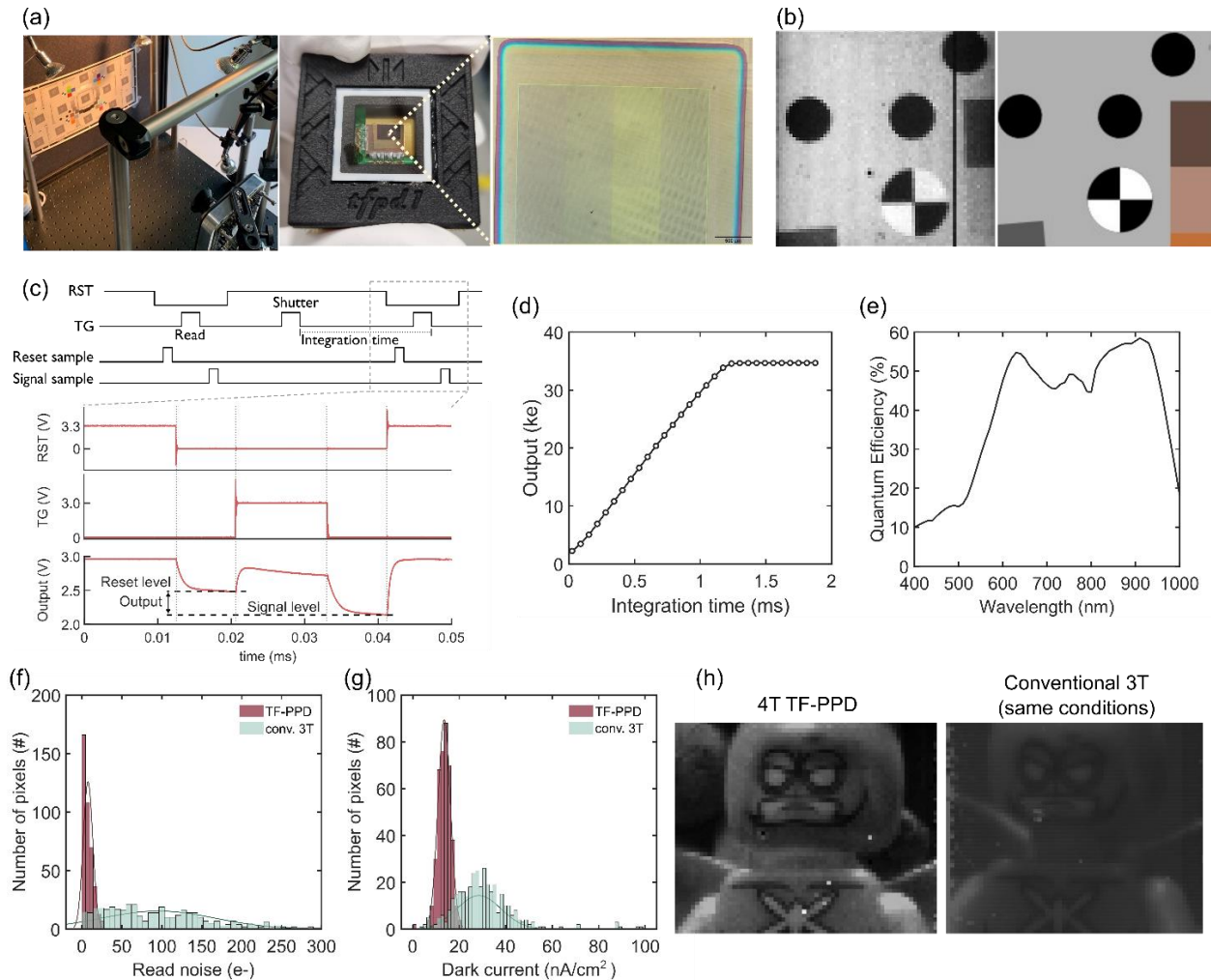
*Figure 5: Image sensor demonstration (a) test camera and processed image sensor; (b) captured uncorrected 64\*64 image with TF-PPD imager (left) and 180\*180 image with commercial camera (right); (c) operation timing diagram and monitored output by oscilloscope; measured (d) output versus integration time and (e) quantum efficiency. Measured pixel statistics of the dark read noise (f) and dark current (g), and (h) sample captured image comparison with the conventional 3T based imager.*

## REFERENCES

1.     Rand, B. P. *et al.* The Impact of Molecular Orientation on the Photovoltaic Properties of a Phthalocyanine/Fullerene Heterojunction. *Adv. Funct. Mater.* **22**, 2987–2995 (2012).

2.     Georgitzikis, E. *et al.* Integration of PbS Quantum Dot Photodiodes on Silicon for NIR Imaging. *IEEE Sens. J.* **20**, 6841–6848 (2020).

3.     Georgitzikis, E. *et al.* Optimization of Charge Carrier Extraction in Colloidal Quantum Dots Short-Wave Infrared Photodiodes through Optical Engineering. *Adv. Funct. Mater.* **28**, 1804502 (2018).

4.     Leemans, J. *et al.* Colloidal III–V Quantum Dot Photodiodes for Short-Wave Infrared

Photodetection. *Adv. Sci.* **9**, 2200844 (2022).

5.    Ackerman, M. M., Tang, X. & Guyot-Sionnest, P. Fast and Sensitive Colloidal Quantum Dot Mid-Wave Infrared Photodetectors. *ACS Nano* **12**, 7264–7271 (2018).

6.    Li, Z. *et al.* Halide perovskites for high-performance X-ray detector. *Mater. Today* **48**, 155–175 (2021).

7.    Nishimura, K. *et al.* An 8K4K-resolution 60fps 450ke--saturation-signal organic-photoconductive-film global-shutter CMOS image sensor with in-pixel noise canceller. *Dig. Tech. Pap. - IEEE Int. Solid-State Circuits Conf.* **61**, 82–84 (2018).

8.    Nishimura, K. *et al.* Advanced features of layered-structure organic-photoconductive-film CMOS image sensor: Over 120 dB wide dynamic range function and photoelectric-conversion-controlled global shutter function. *Jpn. J. Appl. Phys.* **57**, (2018).

9.    Basiricò, L. *et al.* Direct X-ray photoconversion in flexible organic thin film devices operated below 1 v. *Nat. Commun.* **7**, (2016).

10.    van Breemen, A. J. J. M. *et al.* Curved digital X-ray detectors. *npj Flex. Electron.* **4**, 22 (2020).

11.    Tsai, H. *et al.* A sensitive and robust thin-film x-ray detector using 2D layered perovskite diodes. *Sci. Adv.* **6**, (2020).

12.    Goossens, S. *et al.* Broadband image sensor array based on graphene–CMOS integration. *Nat. Photonics* **11**, 366–371 (2017).

13.    Gregory, C., Hilton, A., Violette, K. & Klem, E. J. D.  66-3: Invited Paper: Colloidal Quantum Dot Photodetectors for Large Format NIR, SWIR, and eSWIR Imaging Arrays . *SID Symp. Dig. Tech. Pap.* **52**, 982–986 (2021).

14.    Pejovic, V. *et al.* Infrared Colloidal Quantum Dot Image Sensors. *IEEE Trans. Electron Devices* **69**, (2022).

15.    J. S. Steckel & et Alt. 1.62µm Global Shutter Quantum Dot Image Sensor Optimized for Near and Shortwave Infrared. *IEEE Int. Electron Devices Meet.* 518–521 (2021).

16.    Weckler, G. P. Operation of p-n Junction Photodetectors in a Photon Flux Integrating Mode. *IEEE J. Solid-State Circuits* **2**, 65–73 (1967).

17.    Dyck, R. H. & Weckler, G. P. Integrated arrays of silicon photodetectors for image sensing. *IEEE Trans. Electron Devices* **15**, 196–201 (1968).

18.    Teranishi, N., Kohono, A., Ishihara, Y., Oda, E. & Arai, K. No image lag photodiode structure in the interline CCD image sensor. in *1982 International Electron Devices Meeting* 324–327 (IRE, 1982). doi:10.1109/IEDM.1982.190285.

19.    Fossum, E. R. CMOS image sensors: electronic camera-on-a-chip. *IEEE Trans. Electron Devices* **44**, 1689–1698 (1997).

20.    Chamberlain, S. G. Photosensitivity and Scanning of Silicon Image Detector Arrays. *IEEE J. Solid-State Circuits* **4**, 333–342 (1969).

21.    Fry, P. W., Noble, P. J. W. & Rycroft, R. J. Fixed-pattern noise in photomatrices. *IEEE J. Solid-State Circuits* **5**, 250–254 (1970).

22.     Fossum, E. R. Active pixel sensors: are CCDs dinosaurs? in *Charge-Coupled Devices and Solid State Optical Sensors III* (ed. Blouke, M. M.) vol. 1900 2–14 (1993).

23.     Fossum, E. R. & Hondongwa, D. B. A review of the pinned photodiode for CCD and CMOS image sensors. *IEEE J. Electron Devices Soc.* **2**, 33–43 (2014).

24.     Fossum, E. R., Mendis, S. & Kemeny, S. E. Active pixel sensor with intra-pixel charge transfer. US Patent 5,471,515 (1995).

25.     Stephan, B. *et al.* A Vertically Integrated High Resolution Active Pixel Image Sensor for Deep Submicron CMOS Processes. in *Proc. 1999 IEEE Workshop on CCDs and Advanced Image Sensors* (1999).

26.     Schulze Spuentrup, J. D. *et al.* Thin Film on CMOS Active Pixel Sensor for Space Applications. *Sensors* **8**, 6340–6354 (2008).

27.     Lee, J. *et al.* Imaging in Short-Wave Infrared with 1.82 µm Pixel Pitch Quantum Dot Image Sensor. in *2020 IEEE International Electron Devices Meeting (IEDM)* 16.5.1-16.5.4 (IEEE, 2020). doi:10.1109/IEDM13553.2020.9372018.

28.     Blanksby, A. J., Loinaz, M. J., Inglis, D. A. & Ackland, B. D. Noise performance of a color CMOS photogate image sensor. in *International Electron Devices Meeting. IEDM Technical Digest* vol. 47 205–208 (IEEE, 1997).

29.     Arora, H. *et al.* Amorphous indium-gallium-zinc-oxide as electron transport layer in organic photodetectors. *Appl. Phys. Lett.* **106**, 143301 (2015).

30.     James R. Janesick, Tom Elliott, Stewart Collins, Morley M. Blouke, J. F. Scientific charge -coupled devices. *Opt. Eng.* **26**, 692–714 (1987).

31.     Voznyy, O. *et al.* A Charge-Orbital Balance Picture of Doping in Colloidal Quantum Dot Solids. *ACS Nano* **6**, 8448–8455 (2012).

32.     Pejović, V. *et al.* Photodetectors Based on Lead Sulfide Quantum Dot and Organic Absorbers for Multispectral Sensing in the Visible to Short-Wave Infrared Range. *Adv. Funct. Mater.* **32**, 2201424 (2022).

33.     Bi, Y. *et al.* Infrared Solution-Processed Quantum Dot Solar Cells Reaching External Quantum Efficiency of 80% at 1.35 µm and J sc in Excess of 34 mA cm −2. *Adv. Mater.* **30**, 1704928 (2018).

34.     Kramer, I. J. *et al.* Efficient spray-coated colloidal quantum dot solar cells. *Adv. Mater.* **27**, 116–121 (2015).

35.     Choi, H. T. *et al.* Zero-Dimensional PbS Quantum Dot-InGaZnO Film Heterostructure for Short-Wave Infrared Flat-Panel Imager. *ACS Photonics* **7**, 1932–1941 (2020).

36.     Xu, Yang,  and A. J. T. Image lag analysis and photodiode shape optimization of 4T CMOS pixels. in *Proc. Int. Image Sensor Workshop* 153–157 (2013).

37.     Belmonte, A. *et al.* Capacitor-less, Long-Retention (>400s) DRAM Cell Paving the Way towards Low-Power and High-Density Monolithic 3D DRAM. in *2020 IEEE International Electron Devices Meeting (IEDM)* 28.2.1-28.2.4 (IEEE, 2020). doi:10.1109/IEDM13553.2020.9371900.

38.     Han, L., Yao, S. & Theuwissen, A. J. P. A Charge Transfer Model for CMOS Image Sensors. *IEEE*

*Trans. Electron Devices* **63**, 32–41 (2016).

39. Young Chan Kim *et al.* 1/2-inch 7.2MPixel CMOS Image Sensor with 2.25/spl mu/m Pixels Using 4-Shared Pixel Structure for Pixel-Level Summation. in *2006 IEEE International Solid State Circuits Conference - Digest of Technical Papers* vol. 39 1994–2003 (IEEE, 2006).

40. Kim, H. *et al.* 5.6 A 1/2.65in 44Mpixel CMOS Image Sensor with 0.7µm Pixels Fabricated in Advanced Full-Depth Deep-Trench Isolation Technology. in *2020 IEEE International Solid- State Circuits Conference - (ISSCC)* vols 2020-Febru 104–106 (IEEE, 2020).

41. Mori, M., Katsuno, M., Kasuga, S., Murata, T. & Yamaguchi, T. A 1/4in 2M pixel CMOS image sensor with 1.75 transistor/pixel. in *2004 IEEE International Solid-State Circuits Conference (IEEE Cat. No.04CH37519)* vol. 47 110–111 (IEEE, 2003).

42. Kim, J. H. *et al.* Detailed Characterization of Short-Wave Infrared Colloidal Quantum Dot Image Sensors. *IEEE Trans. Electron Devices* **69**, 2900–2906 (2022).

43. Huggett, A., Silsby, C. & Cami, S. A dual-conversion-gain video sensor with dewarping and overlay on a single chip. in *Digest of Technical Papers - IEEE International Solid-State Circuits Conference* 52-53,53a (IEEE, 2009). doi:10.1109/ISSCC.2009.4977303.

44. Oh, Y. *et al.* A 0.8 µm Nonacell for 108 Megapixels CMOS Image Sensor with FD-Shared Dual Conversion Gain and 18,000e- Full-Well Capacitance. in *2020 IEEE International Electron Devices Meeting (IEDM)* vols 2020-Decem 16.2.1-16.2.4 (IEEE, 2020).

45. Togashi, H. *et al.* Three-layer Stacked Color Image Sensor with 2.0-µm Pixel Size Using Organic Photoconductive Film. in *Technical Digest - International Electron Devices Meeting, IEDM* vols 2019-Decem 16.6.1-16.6.4 (IEEE, 2019).

46. Allen, M., Bessonov, A. & Ryhänen, T. 66-4: Invited Paper: Graphene Enhanced QD Image Sensor Technology. *SID Symp. Dig. Tech. Pap.* **52**, 987–990 (2021).

47. Liu, J. *et al.* A near-infrared colloidal quantum dot imager with monolithically integrated readout circuitry. *Nat. Electron.* **5**, 443–451 (2022).

48. Funatsu, R. *et al.* A 33Mpixel 60fps CMOS image sensor with 32-column shared high-speed column-parallel SAR ADCs. in *2015 IEEE International Solid-State Circuits Conference - (ISSCC) Digest of Technical Papers* vol. 58 1–3 (IEEE, 2015).

49. Oike, Y. *et al.* 8.3 M-Pixel 480-fps Global-Shutter CMOS Image Sensor with Gain-Adaptive Column ADCs and Chip-on-Chip Stacked Integration. *IEEE J. Solid-State Circuits* **52**, 985–993 (2017).

50. Okada, C. *et al.* A 50.1-Mpixel 14-Bit 250-frames/s Back-Illuminated Stacked CMOS Image Sensor With Column-Parallel kT / C -Canceling S&H and ΔΣADC. *IEEE J. Solid-State Circuits* **56**, 3228–3235 (2021).